Tuning the structure and wetting properties of organic-inorganic nanocomposite coatings prepared by aerosol-assisted atmospheric pressure cold plasma deposition

Dr. Fiorenza Fanelli[a,*], Dr. Anna Maria Mastrangelo[b], Dr. Gianvito Caputo[c], Prof. Francesco Fracassi[a,b]

[a] *Institute of Nanotechnology (NANOTEC), National Research Council (CNR), c/o Department of Chemistry, University of Bari "Aldo Moro", via Orabona 4, 70126 Bari, Italy*

[b] *Department of Chemistry, University of Bari "Aldo Moro", via Orabona 4, 70126 Bari, Italy*

[c] *Nanochemistry Department, Istituto Italiano di Tecnologia, via Morego 30, 16163 Genoa, Italy*

* Corresponding author at: Institute of Nanotechnology (NANOTEC), National Research Council, c/o Department of Chemistry, University of Bari "Aldo Moro", via Orabona 4, 70126 Bari, Italy.

E-mail address: fiorenza.fanelli@cnr.it (F. Fanelli).

Phone: +39 0805442227

Fax: +39 0805442227

Abstract

Dispersions of oleate-capped ZnO nanoparticles (NPs) in binary n-octane/1,7-octadiene solvent mixtures are injected, in aerosol form, in a dielectric barrier discharge to deposit hydrocarbon polymer/ZnO nanoparticles nanocomposite (NC) thin films at atmospheric pressure and room temperature. The chemical composition of the coatings, and in turn their morphology and wettability, can be tuned by simply changing the composition of the starting dispersion. Specifically, the increase of the NPs concentration in the dispersion (0.5-5 wt %) results in a continuous increase of both the ZnO content and deposition rate of the coatings. Moreover, when the concentration of 1,7-octadiene in the solvent mixture is very low (0.5-2 vol %), the incorporation of NPs is further promoted, while at concentrations greater than 2 vol % the growth of the organic component starts to be favored. Overall, results reveal a considerable increase of   the root-mean-square (RMS) roughness of the coatings with the ZnO loading. In addition, once the threshold ZnO loading and RMS roughness of 60 wt % and 350 nm are reached, respectively, the coatings are superhydrophobic and exhibit very low water contact angle hysteresis, due to the coexistence of the low surface energy conferred by the hydrocarbon polymer and the hierarchical multiscale surface texture induced by NPs incorporation.

Keywords

atmospheric pressure cold plasma

nanoparticle dispersion

aerosol

organic-inorganic nanocomposite coating

superhydrophobicity

1. Introduction

In the last decade, aerosol-assisted deposition processes, also referred to as spray-deposition or spray-coating processes, have been widely exploited for the preparation of organic-inorganic nanocomposite (NC) coatings combining various inorganic nanoparticles (NPs) and polymers [1,2]. The continuous research in this field is highly motivated by the wealth of structures and properties offered by hybrid materials [3,4] as well as by the fact that aerosol-assisted deposition processes appear to be very promising for large-scale production [2,4]. These processes generally involve the atomization of a dispersion containing preformed inorganic NPs as well as either the preformed polymer [5−7] or the precursors of the polymeric component [8−10]. Both single-step [9−12] and double-step [5,7,8,13,14] strategies have been proposed depending on whether the precursor polymerization and/or curing of the nanocomposite coating occur during or after dispersion atomization. Considerable efforts have been directed towards the fine tuning of the chemical composition, morphology and various functional properties of the deposited coatings, by changing, for instance, the composition of the starting dispersion [5−8,15−19]. For what concerns the wettability of the deposited coatings, previous research suggests that aerosol-assisted strategies enable the facile preparation of superhydrophobic surfaces [2,7−21] characterized by water contact angle (WCA) greater than 150° and contact angle hysteresis less than 10°. These wetting properties can arise from the interplay of a properly selected low surface energy organic component and an adequate surface roughness at the micro- and nanoscale induced by NPs incorporation. It has been shown that low hysteresis superhydrophobic NC coatings can be easily prepared by spray-deposition methods without use of any fluoropolymer or fluorine-containing surface functionalisation agent [2,7−12,20,21]. Indeed, superamphiphobic surfaces [22], exhibiting high contact angles and low contact angle hysteresis to both water and low surface tension liquids, can be also obtained due to the

4

combination of adequate fluorocarbon surface modification and re-entrant texture (i.e., re-entrant surface curvature) induced by nanoparticles agglomeration [5,23,24].

We previously reported on the growth and structure of superhydrophobic organic-inorganic NC thin films deposited by using an aerosol-assisted cold plasma process [9,10,25], in which an atmospheric pressure dielectric barrier discharge (DBD) was fed with a carrier gas and the aerosol of a dispersion of preformed inorganic NPs in a liquid organic precursor [1]. This deposition method allowed the preparation in a single step and at room temperature of hierarchical micro/nanostructured nanocomposite thin films consisting of the NPs and the organic component formed via plasma polymerization of the liquid precursor. Broadly, the versatility of this approach mainly resides in the possibility of combining preformed NPs with in principle any organic precursor (even an unsaturated organic compound), which introduced in the plasma undergoes fragmentation and consequent plasma polymerization [1]. In particular, hydrocarbon polymer/ZnO NPs nanocomposite coatings were deposited from dispersions of oleate-capped ZnO NPs in *n*-octane [9]; the coatings exhibited superhydrophobic behavior due the synergistic effect of the hierarchical multiscale roughness and the low surface energy polymer formed through plasma polymerization of the hydrocarbon solvent.

Very recently, various nanocomposite coatings were deposited using this strategy and considerable progress was made in process understanding [26−32]. Studies were mainly focused on the influence of the atomization conditions [30] as well as of the electrical excitation parameters of the atmospheric pressure cold plasma [27,28,31,32]. For instance, in case of DBDs fed with argon and dispersions of TiO_2 NPs in isopropanol, it was found that the discharge excitation frequency controls the NC coating composition by independently influencing the NPs transport to the substrate surface and the growth of the organic component formed through plasma polymerization of isopropanol [31]. At low frequency (1-10 kHz) the transport of NPs to the surface is favored due to NPs charging and subsequent

electro-deposition (or electro-collection), and dominates over isopropanol plasma polymerization. By increasing the frequency from 10 to 50 kHz the polymer growth rate increases, while NPs remain mainly trapped in the gas phase. Indeed, fine control of the nanocomposite composition, morphology and wetting properties can be achieved by using excitation frequency modulation, i.e., by periodically alternating sinusoidal signals at two frequencies adapted to the NPs transport to the surface (1 kHz) and to the growth of the organic component (15 kHz), respectively [32].

In this work we focus the attention on the composition of the starting dispersion. In particular, we deposited organic/inorganic NC thin films by injecting in an atmospheric pressure plasma the aerosol of a dispersion of oleate-capped ZnO NPs in hydrocarbon (HC) solvent mixtures of *n*-octane and 1,7-octadiene. We found that the chemical composition, morphology and wetting properties of the hybrid coatings can be tuned by simply varying the dispersion composition, in terms of NPs concentration and 1,7-octadiene volume fraction in the HC solvent mixture.

2. Material and methods

Deposition processes were carried out using a home-made atmospheric pressure plasma reactor with parallel plate dielectric barrier discharge (DBD) electrode configuration, as described previously in full detail [9]. The DBD was generated by applying to the electrodes a sinusoidal AC high voltage (22.0 ± 0.2 kHz, 2.6 ± 0.2 kV_{RMS}) in pulsed mode (20 ms period, 13 ms plasma on-time, 65% duty cycle). Under these conditions the DBD operated in filamentary regime and the average specific power dissipated in the discharge was equal to $0.28 ± 0.02$ $W·cm^{-2}$. During the deposition process the plasma was fed by helium (Airliquide, total flow rate of 8000 sccm) and the aerosol of a dispersion of oleate-capped ZnO NPs in hydrocarbon solvents (mass flow rate of $0.23 ± 0.02$ $g·min^{-1}$). Commercial ZnO nanoparticles (ABCR GmbH & Co. KG, 99.5% purity, 36 nm average particle size) were utilized and

surface-functionalized with oleate according to the procedure described elsewhere [9], to obtain stable dispersions in hydrocarbon solvents. Specifically, in this work, dispersions of oleate-capped ZnO NPs in binary solvent mixtures of n-octane (Sigma-Aldrich, purity $\geq$ 99.0%,) and 1,7-octadiene (Sigma-Aldrich, 98% purity) were utilized. The concentration of NPs ([NPs]) in the dispersions was varied in the range $0.5 - 5$ wt %, while the concentration of 1,7-octadiene ([1,7-octadiene]) in the binary HC mixture was increased up to 10 vol %. Thin films were deposited for 10 min on various substrates (i.e., borosilicate glass slides, CaF_2 substrates, carbon-coated Cu grids) placed in the middle of the discharge region, onto the alumina plate covering the lower electrode. The temperature of the alumina plate increases from room temperature to about 80 °C during the first 5 min of the plasma process, then it maintains this value for longer deposition times.

X-ray photoelectron spectroscopy (XPS) analyses were carried out using a Thermo Fisher Scientific Theta Probe spectrometer equipped with a monochromatic Al Ka X-ray source (300 μm spot size, 70 W power) and a flood gun to balance the surface charging. Spectra were recorded at a take-off angle of 37° with respect to the sample surface, using a pass energy of 200 eV and 100 eV for survey and high resolution regions (C 1s, O 1s, and Zn 2p), respectively. Data analysis and curve-fitting were performed by the commercial Thermo Avantage v5.938 software (Thermo Fisher Scientific) [9]. The calibration of the binding energy (BE) scale was performed by taking the aliphatic hydrocarbon component (C-C/C-H, BE = 285.0 eV) of the C 1s spectrum as internal reference. XPS analyses were carried out on three samples produced in different experiments (three analyzed spots per sample).

A vacuum Fourier transform infrared (FTIR) spectrometer was used to collect the infrared absorption spectra of the thin films deposited on CaF_2 substrates in attenuated total reflectance (ATR) mode (diamond ATR crystal). The ATR-FTIR spectra of the coatings, obtained by subtracting the CaF_2 substrate spectrum, were baseline corrected and normalized to the most intense absorption band (unless otherwise specified).

The ZnO loading in the nanocomposites, defined as weight percentage (wt %) of ZnO, was determined by measuring the Zn concentration with anodic stripping voltammetry (ASV), after wet acid digestion of weighed amount of NC coating as described previously in full detail [9]. Measurements were repeated on five samples and average loading values were calculated.

X-ray diffraction (XRD) analyses of pristine ZnO NPs, oleate-capped ZnO NPs and NC coatings were performed on a PANalytical Emyprean X-Ray diffractometer using a Cu Kα anode (λ = 1.5406 Å) operating at 45 kV and 40 mA. The diffraction patterns were collected in the range 10–70° 2θ with a 0.01° step size.

A Zeiss SUPRA™ 40 field emission scanning electron microscope (FESEM) was used for the morphological investigation. SEM images were acquired at the electron acceleration voltage (extra-high tension, EHT) of 2 kV (unless otherwise specified) using a high resolution in-lens secondary electron detector. Samples were sputter-coated with a 10 nm thick layer of Cr prior to SEM analyses. Transmission scanning electron microscopy (TSEM) observations were carried out on NC coatings directly deposited onto carbon-coated copper grids (deposition time = 1 min), utilizing the multimode TSEM detector in dark-field (DF) mode (EHT = 20 kV).

White light vertical scanning interferometry (WLVSI) was utilized to determine the thickness and the route mean square (RMS) surface roughness of the coatings. Analyses were carried out with a Bruker Contour GT-K0X three-dimensional (3D) optical microscope equipped with a 50x Mirau-type inteferometric objective and a 0.55x camera zoom (0.17 x 0.23 mm^2 field of view). The reported thickness and RMS roughness values are the mean of measurements on three samples produced in different experiments (measurements at five different locations per sample); roughness measurements were carried out over 0.17 x 0.23 mm^2 surface areas.

The mass deposition rate of the coatings, expressed in units of mass per unit time per unit area, was calculated by dividing the weight of the NC deposited onto glass substrates (measured by a Mettler Toledo XS205 analytical balance) by the deposition time and the substrate area. The mass deposition rates of the organic and inorganic components of the NC were calculated from the mass deposition rate of the NC coating and the ZnO loading determined by ASV measurements after coating digestion.

Dynamic WCA measurements were carried out with Ramé-Hart manual goniometer (model A-100) using the sessile drop method, in order to assess advancing and receding contact angles as well as the contact angle hysteresis, defined as the difference between the advancing and receding contact angles. WCA measurements were performed on three samples produced in different experiments (measurements at five different locations per sample).

The adhesion of the coatings to glass substrates was evaluated by tape test based on the ASTM standard (i.e., D3359 standard test methods for rating adhesion by tape test) [34,35]. In the test, the tape (3M Scotch 810 Magic Tape) was pressed against the coating with a fingertip and, after 60 s, it was pulled off rapidly back at an angle as close as possible to 180°. WCA measurements and SEM analyses were carried out before and after the peel adhesion test.

A stainless steel liquid nitrogen trap, located between the reactor and the pump was employed to sample the stable species contained in the exhaust gas of the plasma process [36,37], i.e., unreacted n-octane and 1,7-octadiene, and byproducts formed through plasma activation. The sampling was performed for 5 min, then the trap was isolated, the condensate was dissolved in acetone (Sigma–Aldrich, 99.8% purity) and, finally, the solution was filtered and analyzed by gaschromatography-mass spectrometry (GC-MS). The gaschromatograph (GC 8000Top Thermoquest Corporation) was equipped with a Agilent J&W HP-5ms Ultra Inert GC column (30 m length, 0.25 mm internal diameter of 0.25 mm) characterized by a (5%-Phenyl)-methylpolysiloxane stationary phase (0.25 μm thickness). GC analyses were carried out using

He as carrier gas (1 sccm), at 250 °C injector temperature and a column temperature programmed from 30 to 200 °C (2 min at 30 °C, 10 °C·min⁻¹, 5 min at 200 °C). Separated products were analyzed using a quadrupole mass spectrometer (Voyager, Finnigan, Thermoquest Corporation) operating at the standard ionizing electron energy of 70 eV and at the interface and source temperature of 250°C; spectra were recorded in full-scan mode in the mass-to-charge ratio in the range 15 – 500. Stable products were identified by means of MS available libraries [38]; products identification was confirmed by comparison of retention time and mass spectrum with standard compounds. The quantitative analysis of some identified species was performed utilizing cyclohexane (Sigma-Aldrich, 99.8% purity) as internal standard (IS) through calibration curves in the linear range. The amounts of quantified compounds are expressed as mass flow rate (in $g \cdot min^{-1}$ or $\mu g \cdot min^{-1}$) obtained by dividing the mass of the collected species by the sampling time. The extent of reacted n-octane and 1,7-octadiene (i.e., hydrocarbon precursor depletion percentage) was calculated according to Eq. (1):

$$\text{Depletion \%} = \frac{MFR_{OFF} - MFR_{ON}}{MFR_{OFF}} \cdot 100 \qquad (1)$$

where MFR_{OFF} MFR_{ON} are hydrocarbon precursor mass flow rates detected in the exhaust in plasma off and plasma on conditions, respectively.

3. Results and discussion

The growth and structure of the NC coating were investigated, first of all, by varying the concentration of oleate-capped ZnO NPs in the starting dispersion from 0.5 to 5 wt %, while keeping constant the composition of the *n*-octane/1,7-octadiene solvent mixture ([1,7-octadiene] = 0.5 vol %).

Fig. 1a shows the attenuated total reflectance-Fourier transform infrared (ATR-FTIR) spectra of the NC coatings obtained from dispersions at NPs concentrations of 0.5, 3 and 5 wt % in the HC mixture. The spectra present the characteristic absorptions of both the oleate-capped

ZnO NPs and the organic component formed via plasma polymerization of *n*-octane and 1,7-octadiene [9]. They, in fact, show the ZnO absorption band (420 cm^{-1}) and the asymmetric and symmetric stretching signals of carboxylate groups (in the range 1300−1600 cm^{-1}) ascribed to the oleate-capped ZnO NPs [9,39]. In addition, the CH_2 and CH_3 stretching and bending signals (2800−3000 and 1300−1600 cm^{-1}, respectively) are in good agreement with the corresponding bands observed in the case of the polyethylene-like coating deposited from a n-octane/1,7-octadiene aerosol (without NPs) [9,40]. Nanocomposite ATR-FTIR spectra do not display any appreciable olefinic C-H signal (Fig. S1), typical of the =C−H stretching mode in oleate (3005 cm^{-1}) as well as of the various stretching vibrations of vinyl groups in 1,7-octadiene (in the range 2970-3100 cm^{-1}) [9,40].

The intensity ratio between the ZnO and the CH_x absorption bands in the spectra of the NC coatings increases by increasing the concentration of the oleate-capped ZnO NPs in the starting dispersion from 0.5 to 5 wt % (Fig. 1a). This trend is also confirmed by the considerable increase of the ZnO loading in the coatings from 26 ± 4 wt % to 78 ± 5 wt %, (Fig. 1b), as determined by anodic stripping voltammetry (ASV) after coating digestion. It is worth mentioning that the ZnO content in the oleate-capped NPs is 95.0 ± 1.0 wt %.

Fig. 1c shows the increase of the mass deposition rate of the coatings as a function of the NPs concentration in the dispersion. Interestingly, this increase seems to reflect the trend of the mass deposition rate of the inorganic components of the NC, since the mass deposition rate of the organic component remains quite constant with NPs concentration.

X-ray photoelectron spectroscopy (XPS) analyses revealed that, by increasing the NPs content in the starting dispersion from 0.5 to 5 wt %, the surface atomic concentrations of Zn and O increase from $0.50 \pm 0.10\%$ to $8.0 \pm 1.0\%$ and from $3.0 \pm 0.5\%$ to $16 \pm 2\%$, respectively. On the other hand, a concomitant decrease of the C atomic concentration from 96.5 ± 1.0 % to $76 \pm 3\%$ is observed. The surface atomic concentrations of C, O and Zn in case of oleate-capped NPs are about 55%, 29% and 16%, respectively [9]. The typical high-resolution C 1s

spectrum of the hybrid coating, reported in Fig. 2a, is curve-fitted with two peaks: the main peak at 285.0 eV ascribed to the aliphatic hydrocarbon component and the low intensity peak due to C−O at about 286.5 eV (peak area percentage less than 5%). Differently, as reported in ref. [9], the C1s signal of the oleate-capped NPs is curve-fitted with the C−C/C−H (285.0 eV, ~95%) and COO (288.8 eV, ~5%) components, in agreement with oleate chemical structure. The high-resolution O1s spectrum of the NC coating in Fig. 2a displays two components belonging to different oxygen environments, i.e., ZnO (530.2 eV, 65%) and C-O/O-H (532.1 eV, 35%), respectively. Finally, the Zn $2p_{3/2}$ signal of the nanocomposite is symmetrical and centered at 1021.8 eV, as reported for ZnO [41], and presents a very slight shift towards higher BE with respect to the oleate-capped NPs.

X-ray diffraction (XRD) investigation on the nanocomposites pointed out that ZnO NPs crystallinity was not affected by the deposition process (Fig. 2b, Figs. S2 and S3). As a matter of fact, the typical reflections of ZnO in wurtzite crystal habit (JPCDS card 36-1451) are present in the XRD spectra of both the NC coatings and of the oleate-capped ZnO NPs reported in Fig. 2b. Moreover, the amorphous band between 10 and 30° can be assigned to the contribution of the glass substrate on which the nanocomposite coatings were deposited (Figs. 2b and S3).

Top-view and cross-sectional scanning electron microscopy (SEM) images are reported in Fig. 3, and show that, by increasing the NPs concentration in the starting dispersion, a transition from a polymer-dominated to a nanoparticles-dominated morphology occurs. In particular, while the coating deposited from a 0.5 wt % NPs dispersion exhibits a relatively smooth morphology (Fig. 3a), a hierarchical microscale-to-nanoscale morphology appears for higher NPs concentrations, due to the presence of quasi-spherical NPs agglomerates with minimum and maximum size of about 200 and 2000 nm, respectively (Figs. 3b). The change in coatings morphology with the NPs concentration in the dispersion, and in turn with the ZnO loading in the coatings, is also accompanied by a remarkable increase of the root-mean-

square (RMS) roughness from ∼200 nm to ∼1000 nm. Interestingly, the formation of analogous NPs agglomerates was widely reported and discussed in the literature on aerosol-assisted processes involving the atomization of NPs dispersions [5,7,9,17,27,29−32]. The SEM and dark-field TSEM (transmission scanning electron microscopy) images in Fig. 4a clearly evidence the densely-packed structure of the NPs agglomerates, covered by a thin organic layer with thickness ranging from a few nm to *ca.* 20 nm [9]. The presence of this organic layer may explain why the surface atomic composition of the NC coatings determined by XPS (maximum sampling depth of ∼10 nm) is dominated by the hydrocarbon polymer, in spite of the high ZnO content of the coatings assessed by ASV after coating digestion (Fig. 1b). In addition, the morphological investigation reveals that the organic component could play as structuring agent of the three-dimensional (3D) network of the hybrid coating, holding together the NPs agglomerates, while ensuring their adhesion to the substrate (*cf.* cross-sectional SEM images in Fig. 3).

In agreement with the trend of the mass deposition rate (Fig. 1c), white light vertical scanning interferometry (WLVSI) measurements revealed that, for a deposition time of 10 min, the thickness of the coatings varies from 320 ± 30 nm to 4500 ± 400 nm by increasing the NPs concentration in the dispersion from 0.5 to 5 wt %, as also confirmed by cross-sectional SEM images (Fig. 3).

Overall, the following three evidences suggest the preferential collection of NPs on the substrate surface during the deposition process, which becomes even more evident when the NPs concentration in the dispersion is increased: (i) the high ZnO loading levels reached in the coatings, as compared to the NPs weight percentage in the starting dispersions; (ii) the trend of the mass deposition rate of the inorganic component with respect to the organic counterpart; (iii) the appearance of a coating morphology severely dominated by the NPs agglomerates. In agreement with previous works, NPs deposition during this plasma process could be due to charging of NPs agglomerates in the atmospheric plasma and subsequent

electro-collection on the substrate surface [27,28,31,32,42,43]. Moreover, considering the excitation frequency (22 kHz) and pulsed plasma conditions used in this work, NPs deposition mainly occurring when the plasma is off is a likely scenario [27,28,31,32].

The NPs content in the starting dispersion significantly affects also the wettability of the hybrid coatings. In particular, with increasing the NPs concentration from 0.5 to 5 wt %, advancing and receding WCAs increase from $111 \pm 2°$ to $170 \pm 3°$ and from $73 \pm 3°$ and $168 \pm 2°$, respectively. Therefore, superhydrophobic surfaces (i.e., advancing and receding contact angles greater than 150°) with very low hysteresis are obtained when the concentration of NPs in the dispersion is greater or equal to 1 wt %. This wettability behavior derives from the synergistic effect of the hierarchical multiscale surface texture due to NPs incorporation and the low surface energy hydrocarbon polymer.

Since, under the experimental conditions utilized in this work, the DBD operated in filamentary regime, it is worth specifying that the coatings exhibited good uniformity in terms of chemical composition, morphology and wettability behavior. Moreover, SEM observations did not evidence non-uniformities and damages that could be ascribed to discharge localization and microdischarges formation (e.g., microdischarges footprints) during coating deposition.

In the second part of this study the structure and wetting properties of the NC coating were investigated, by varying the composition of the *n*-octane/1,7-octadiene solvent mixture of the starting dispersion. In particular the concentration of 1,7-octadiene was increased up to 10 vol %, while keeping constant the of oleate-capped ZnO NPs content at 3 wt %.

Fig. 5a shows that the ZnO loading in the coatings slightly increases from 68 ± 3 wt %, in case of a dispersion in pure *n*-octane, to about 75 wt % for 1,7-octadiene concentration in the HC mixture up to 2 vol %. Then, when the 1,7-octadiene fraction is further increased, the ZnO loading starts to continuously decrease to the final value of about 45 wt %, as obtained at the maximum 1,7-octadiene concentration of 10 vol %. The trend of the ZnO loading is

confirmed by the evolution of the relative intensities of the infrared absorptions of the NC coatings with the 1,7-volume percentage (Fig. S4). XPS results as a function of HC solvent mixture composition confirmed that the surface composition of the coatings is dominated by the hydrocarbon polymer. Specifically, the XPS atomic concentration of C varies between 85 - 95 %, while the Zn and O atomic concentrations do not exceed the 5 % and 10 %, respectively.

As reported in Fig. 5b, the mass deposition rate of the NC coatings varies in the range 0.20 – 0.26 $\mu g \cdot mm^{-1} \cdot min^{-1}$ and reaches its maximum at 1 vol % 1,7-octadiene. Interestingly, the trends of the mass deposition rates for the organic and inorganic components support the preferential growth of the inorganic component when the concentration of 1,7-octadiene in the HC mixture is very low (maximum at 1 vol % 1,7-octadiene), since the deposition rate of the polymeric counterpart remains low and quite constant. Then, at 1,7-octadiene concentration greater than 2 vol %, the mass deposition rate of the organic polymer starts to increase and, eventually, prevails over the inorganic component.

On the basis of these results, it seems that 1,7-octadiene addition is able to trigger the growth of the organic and inorganic components of the NC coating, due to the high reactivity conferred by the two terminal carbon-carbon double bonds. Specifically, 1,7-octadiene apparently increases the sticky probability of NPs and NPs agglomerates, favoring their immobilization on the substrate surface, when added in the HC mixture at very low concentrations. On the other hand, by further increasing the 1,7-octadiene concentration, the growth of the NC organic component is promoted since 1,7-octadiene is an unsaturated hydrocarbon significantly more prone to plasma polymerization than n-octane.

To gain insights into the deposition mechanism and to enlighten the different reactivity of n-octane and 1,7-octadiene, the GC-MS investigation of the organic species present in the exhaust of the plasma processes was carried out as a function of the 1,7-octadiene concentration in the dispersion solvent mixture. First of all, it was observed that the amount of

reacted n-octane remains very low and constant with the HC mixture composition (i.e., reacted mass flow rate of about 6 ± 1 mg·min^{-1} corresponding to a n-octane depletion of *ca.* 3%). On the other hand, the reacted 1,7-octadiene amount increases from *ca.* 0.8 mg·min^{-1} to *ca.* 8 mg·min^{-1} by increasing the 1,7-octadiene concentration from 0.5 to 10 vol % (corresponding to a 1,7-octadiene depletion of about 70% and 35%, respectively). Results from the qualitative and quantitative determination of byproducts formed through plasma activation are provided in the Supporting Material. Briefly, in case of a dispersion of NPs in n-octane (no 1,7-octadiene addition), identified byproducts include mainly linear and branched alkanes and alkenes containing from 6 to 13 carbon atoms (C6-C13), present in the exhaust at mass flow rates ranging between 15 µg·min^{-1} and 250 µg·min^{-1} (Fig. S5a). Interestingly, the most abundant species are some octene isomers (i.e., 1-octene, trans-2-octene, cis-2-octene); while, with increasing the number of carbon atoms in the byproduct molecule from 8 to 13 a continuous decrease of the byproducts produced amount is observed. Two oxygen containing species are also present (i.e., 3-octanol and 3-octanone). Their formation could be due to the reaction of hydrocarbon fragments with oxygen and water vapor contaminations and/or with oleate-capped ZnO NPs. When 10 vol % 1,7-octadiene is added to the HC mixture, the quali-quantitative distribution of linear and branched alkanes and alkenes does not change significantly (Fig. S5b), however the formation of new cyclic hydrocarbons is observed (Fig. S5c).

SEM images displayed in Figs. 6 and S6 show that, at very low 1,7-octadiene concentration, the deposition of hierarchical micro/nanostructured coatings containing quasi-spherical NPs agglomerates is favored and the average thickness of the coatings increases with respect to a dispersion in pure *n*-octane (thickness of about 2500 nm at 1 vol % 1,7-octadiene for a deposition time of 10 min). Moreover, at 1,7-octadiene concentration of 3 vol %, the growth of the organic component starts to compete, and the presence of the hydrocarbon polymer layer covering the NPs agglomerates can be clearly detected in the corresponding SEM

images (Figs. 6c and S6c). Finally, at the maximum 1,7-octadiene concentration of 10 vol %, NPs agglomerates appear to be almost completely embedded in the hydrocarbon polymer matrix (Figs. 6d and S6d). In addition, TSEM images show densely packed NPs agglomerates for coatings deposited from dispersions at low 1,7-octadiene concentration (*cf.* Figs. 4a and b corresponding to 1,7-octadiene concentration of 0.5 and 2 vol %). On the other hand, it should be worthy to note that by increasing 1,7-octadiene volume fraction the agglomerates structure is affected and a certain spreading seems to occur (e.g., Fig. 4c, 10 vol % 1,7-octadiene).

The trend of the RMS roughness reported in Fig. 6e can be related to the evolution of the coatings morphology with the composition of the dispersion solvent mixture. Specifically, the RMS roughness reaches its maximum at 1 vol % 1,7-octadiene (about 900 nm) and decreases down to 250 nm for a 10 vol % 1,7-octadiene content. On the other hand, Fig. 6f shows that both advancing and receding WCAs decrease with the 1,7-octadiene concentration, while the contact angle hysteresis increases. In particular, superhydrophobic coatings with low contact angle hysteresis are obtained at 1,7-octadiene concentration less than or equal to 3 vol %. Above this threshold concentration advancing and receding WCA values are about 110 and 70°, respectively, and WCA hysteresis is about 40°.

No changes in chemical composition, morphology and wettability of the coatings were observed after ageing for 6 months under ambient conditions. Moreover, NC coatings maintained the low hysteresis superhydrophobic behavior also after 24 h of water immersions. To assess whether the superhydrophobic micro/nanostructured NC coatings adhere to glass substrates, the tape peel test [34,35] was performed on thin films deposited from dispersions at 1,7-octadiene concentration in the range 0 − 3 vol % (3 wt % NPs). SEM investigation proved that the thickness of the coatings decreases after peel test, due to NPs agglomerates removal (Figs. S7a,b). Nevertheless, WCA measurements showed that NC

coatings deposited from a dispersion at the optimum 1 vol % 1,7-octadiene concentration maintain the low hysteresis superhydrophobic character after peel test (Figs. S7c,d).

Fig. 7a summarizes all the results obtained in this work and, specifically, reveals an considerable increase of the RMS roughness with the ZnO loading in the NC coatings deposited in DBDs fed with helium and the aerosol of dispersions of oleate-capped ZnO NPs in n-octane/1,7-octadiene mixtures. Moreover, Fig. 7b shows that once the threshold ZnO loading of 60 wt % is reached, corresponding to a threshold RMS roughness of 350 nm, the coatings exhibit superhydrophobic behavior accompanied by low contact angle hysteresis.

4. Conclusion

In this work, hydrocarbon polymer/ZnO nanoparticles NC coatings were deposited by using an aerosol-assisted cold plasma process, in which the aerosol of a dispersion of oleate-capped ZnO NPs in n-octane/1,7-octadiene solvent mixtures is injected in a dielectric barrier discharge at atmospheric pressure. A comprehensive study of the influence of the dispersion composition is presented, to demonstrate the possibility of tuning the structure and wetting properties of the hybrid coatings. The increase of the NPs concentration in the starting dispersion leads to a continuous increase of the ZnO loading in the coatings. On the other hand, 1,7-octadiene addition favors the immobilization of NPs agglomerates on the substrate surface at low concentrations in the HC mixture (up to 2 vol %), while boosts the growth of the organic component at higher concentrations. Summarizing all the data obtained in this work, we found that the RMS roughness of the coatings significantly increases with the ZnO loading. Interestingly, low hysteresis superhydrophobic coatings are obtained above the threshold ZnO loading and RMS roughness of 60 wt % and 350 nm, respectively. The spatial distribution of the organic and inorganic components of the hybrid layer explains this wetting behavior, i.e., the low surface energy hydrocarbon polymer dominates the surface chemical

18

composition of the NC coating, while NPs form quasi-spherical agglomerates inducing a hierarchical multiscale surface texture. The results reported herein confirm aerosol-assisted cold plasma deposition as a viable strategy towards the preparation of hybrid coatings with extreme wetting properties. Future work will involve extending the deposition method to the production of superamphiphobic NC coatings, acting in particular on the chemical composition of the organic component.

Supplementary Material

ATR-FTIR spectra of liquid hydrocarbons, hydrocarbon solvent mixtures and NC coatings; XRD diffractograms of pristine ZnO NPs, oleate-capped ZnO NPs, various NC coatings, glass substrate; additional SEM images of NC coatings.

References

[1]   F. Fanelli, F. Fracassi, Aerosol-assisted atmospheric pressure cold plasma deposition of organic–inorganic nanocomposite coatings, Plasma Chem. Plasma Process. 34 (2014) 473–487.

[2]   S. Das, S. Kumar, S. K. Samal, S. Mohanty, S. K. Nayak, A Review on superhydrophobic polymer nanocoatings: recent development and applications, Ind. Eng. Chem. Res. 57 (2018) 2727−2745.

[3]   C. Sanchez, B. Julián, P. Belleville, M. Popall, Applications of hybrid organic–inorganic nanocomposites, J. Mater. Chem. 15 (2005) 3559–3592.

[4]   P. Marchand, I. A. Hassan, I. P. Parkin, C. J. Carmalt, Aerosol-assisted delivery of precursors for chemical vapour deposition: expanding the scope of CVD for materials fabrication, Dalton Trans. 42 (2013) 9406–9422.

[5]   A. Steele, I. Bayer, E. Loth, Inherently superoleophobic nanocomposite coatings by spray atomization, Nano Lett. 9 (2009) 501–505.

[6]   F. Zhang, H. Qian, L. Wang, Z. Wang, C. Du, X. Li, D. Zhang, Superhydrophobic carbon nanotubes/epoxy nanocomposite coating by facile one-step spraying, Surf. Coat. Technol. 341 (2018) 15–23.

[7]   P. N. Manoudis, I. Karapanagiotis, A. Tsakal, I. Zuburtikudis, C. Panayiotou, Superhydrophobic composite films produced on various substrates, Langmuir 24 (2008) 11225−11232.

[8]   B. J. Sparks, E. F. T. Hoff, L. Xiong, J. T. Goetz, D. L. Patton, Superhydrophobic hybrid inorganic−organic thiol-ene surfaces fabricated via spray-deposition and photopolymerization, ACS Appl. Mater. Interfaces 8 (2013) 1811–1817.

[9]   F. Fanelli, A. M. Mastrangelo, F. Fracassi, Aerosol-assisted atmospheric cold plasma deposition and characterization of superhydrophobic organic–inorganic nanocomposite thin films, Langmuir 30 (2014) 857−865.

[10]   F. Fanelli, A. M. Mastrangelo, N. De Vietro, F. Fracassi, Preparation of multifunctional superhydrophobic nanocomposite coatings by aerosol-assisted atmospheric cold plasma deposition, Nanosci. Nanotechnol. Lett. 7 (2015) 84−88.

[11]   C. R. Crick, J. C. Bear, A. Kafizas, I. P. Parkin, superhydrophobic photocatalytic surfaces through direct incorporation of titania nanoparticles into a polymer matrix by aerosol assisted chemical vapor deposition, Adv. Mater. 24 (2012) 3505–3508.

[12]   C. R. Crick, J. C. Bear, P. Southern, I. P. Parkin, a general method for the incorporation of nanoparticles into superhydrophobic films by aerosol assisted chemical vapour deposition, J. Mater. Chem. A 1, (2013) 4336–4344.

[13]   H. Wang, E. Chen, X. Jia, L. Liang, Q. Wang, superhydrophobic coatings fabricated with polytetrafluoroethylene and SiO_2 nanoparticles by spraying process on carbon steel surfaces, Appl. Surf. Sci. 349 (2015) 724–732.

[14]   H. Ye, L. Zhu, W. Li, H. Liu, H. Chen, Constructing fluorine-free and cost-effective superhydrophobic surface with normal-alcohol-modified hydrophobic SiO_2 nanoparticles, ACS Appl. Mater. Interfaces 9 (2017) 858−867.

[15] M. K. Tiwari, I. S. Bayer, G. M. Jurisch, T. M. Schutzius, C. M. Magaridis, Highly liquid-repellent, large-area, nanostructured poly(vinylidene fluoride)/poly(ethyl 2-cyanoacrylate) composite coatings: particle filler effects, ACS Appl. Mater. Interfaces 2 (2010) 1114–1119.

[16] A. Raza, Y. Si, X. Wang, T. Ren, B. Ding, J. Yu, S. S. Al-Deyabd, Novel fluorinated polybenzoxazine–silica films: chemical synthesis and superhydrophobicity, RSC Adv., 2 (2012) 12804–12811.

[17] S. G. Lee, D. S. Ham, D. Y. Lee, H. Bong, K. Cho, Transparent superhydrophobic/translucent superamphiphobic coatings based on silica–fluoropolymer hybrid nanoparticles, Langmuir 29 (2013) 15051–15057.

[18] W. S. Y. Wong, Z. H. Stachurski, D. R. Nisbet, A. Tricoli, Ultra-durable and transparent self-cleaning surfaces by large-scale self-assembly of hierarchical interpenetrated polymer networks, ACS Appl. Mater. Interfaces 8 (2016) 13615–13623.

[19] Y.-Q. Qing, C.-N. Yang, Y. Shang, Y.-Z. Sun, C.-S. Liu, Facile approach in fabricating hybrid superhydrophobic fluorinated polymethylhydrosiloxane/TiO$_2$ nanocomposite coatings, Colloid Polym. Sci. 293 (2015) 1809–1816.

[20] J. Meng, S. Lin, X. Xiong, Preparation of breathable and superhydrophobic coating film via spray coating in combination with vapor-induced phase separation, Prog. Org. Coat. 107 (2017) 29–36.

[21] D. Zhi, Y. Lu, S. Sathasivam, I. P. Parkin, X. Zhang, Large-scale fabrication of translucent and repairable superhydrophobic spray coatings with remarkable mechanical, chemical durability and UV resistance, J. Mat. Chem. A 5 (2017) 10622–10631.

[22] J. Yong, F. Chen, Q. Yang, J. Huo, X. Hou, Superoleophobic surfaces, Chem. Soc. Rev. 46 (2017) 4168–4217.

[23] R. Campos, A. J. Guenthner, A. J. Meuler, A. Tuteja, R. E. Cohen, G. H. McKinley, T. S. Haddad, J. M. Mabry, Superoleophobic surfaces through control of sprayed-on stochastic topography, Langmuir 28 (2012) 9834–9841.

[24] L. Xiong, L. L. Kendrick, H. Heusser, J. C. Webb, B. J. Sparks, J. T. Goetz, W. Guo, C. M. Stafford, M. D. Blanton, S. Nazarenko, D. L. Patton, Spray-deposition and photopolymerization of organicinorganic thiol–ene resins for fabrication of superamphiphobic surfaces, ACS Appl. Mater. Interfaces 6 (2014) 10763–10774.

[25] F. Fanelli, P. Bosso, A. M. Mastrangelo, F. Fracassi, Thin film deposition at atmospheric pressure using dielectric barrier discharges: advances on three-dimensional porous substrates and functional coatings, Jpn. J. Appl. Phys. 55 (2016) 07LA01.

[26] J. Profili, O. Levasseur, J.-B. Blaisot, A. Koronai, L. Stafford, N. Gherardi, Nebulization of nanocolloidal suspensions for the growth of nanocomposite coatings in dielectric barrier discharges, Plasma Process. Polym. 13 (2016) 981–989.

[27] J. Profili, O. Levasseur, N. Naudé, C. Chaneac, L. Stafford, N. Gherardi, Influence of the voltage waveform during nanocomposite layer deposition by aerosol-assisted atmospheric pressure Townsend discharge, J. Appl. Phys. 120 (2016) 053302.

[28] J. Profili, S, Dap, O. Levasseur, N. Naudé, A. Belinger, L. Stafford, N. Gherardi, Interaction of atomized colloid with an ac electric field in a dielectric barrier discharge reactor used for deposition of nanocomposite coatings, J. Phys. D: Appl. Phys. 50 (2017) 075201.

[29] J. Profili, O. Levasseur, A. Koronai, L. Stafford, N. Gherardi, Deposition of nanocomposite coatings on wood using cold discharges at atmospheric pressure, Surf. Coat. Technol. 309 (2017) 729–737.

[30] P. Brunet, R. Rincón, J. Margot, F. Massines, M. Chaker, Deposition of homogeneous carbon-TiO_2 composites by atmospheric pressure DBD, Plasma Process. Polym. 14 (2017) 1600075.

[31] P. Brunet, R. Rincón, J.-M. Martinez, Z. Matouk, F. Fanelli, M. Chaker, F. Massines, Control of composite thin film made in an Ar/isopropanol/TiO_2 nanoparticles dielectric barrier discharge by the excitation frequency, Plasma Process. Polym. 14 (2017) 1700049.

[32] P. Brunet, R. Rincón, Z. Matouk, M. Chaker, F. Massines, Tailored waveform of dielectric barrier discharge to control composite thin film morphology, Langmuir 34 (2018) 1865–1872.

[33] G. Beamson, D. Briggs, High Resolution XPS of Organic Polymers; J. Wiley & Sons, Chichester, 1992.

[34] S. Sethi, A. Dhinojwala, Superhydrophobic conductive carbon nanotube coatings for steel, Langmuir 25 (2009) 4311–4313.

[35] S.-M. Lee, K.-S. Kim, E. Pippel, S. Kim, J.-H. Kim, H.-J. Lee, Facile route toward mechanically stable superhydrophobic copper using oxidation-reduction induced morphology changes. J. Phys. Chem. C 116 (2012) 2781–2790.

[36] F. Fanelli, R. d'Agostino, F. Fracassi, GC-MS investigation of hexamethyldisiloxane–oxygen fed cold plasmas: low pressure versus atmospheric pressure operation, Plasma. Process. Polym. 8 (2011) 932–941.

[37] F. Fanelli, S. Lovascio, R. d'Agostino, F. Fracassi, Insights into the atmospheric pressure plasma-enhanced chemical vapor deposition of thin films from methyldisiloxane precursors, Plasma. Process. Polym. 9 (2012) 1132–1143.

[38] NIST and Wiley libraries in MassLab Release 1.4 (GC/MS Data System Software Finnigan).

[39] G. B. Deacon, R. J. Phillips, Relationships between the carbon-oxygen stretching frequencies of caboxylato complexes and the type of carboxylate coordination, Coord. Chem. Rev. 33 (1980) 227–250.

[40]   J. Robertson, Diamond-like amorphous carbon, Mat. Sci. Eng. R 37 (2002) 129–281.

[41]   D. Barreca, A. Gasparotto, C. Maccato, C. Maragno, E. Tondello, ZnO nanoplatelets obtained by chemical vapor deposition, studied by XPS, Surf. Sci. Spectra 14 (2007) 19–26.

[42]   J. P. Borra, Nucleation and aerosol processing in atmospheric pressure electrical discharges: powders production, coatings and filtration, J. Phys. D Appl. Phys. 39 (2006) R19–R54.

[43]   N. Jidenko, C. Jimenez, F. Massines, J. P. Borra, Nano-particle size-dependent charging and electro-deposition in dielectric barrier discharges at atmospheric pressure for thin SiO_x film deposition, J. Phys. D: Appl. Phys. 40 (2007) 4155−4163.

Figure captions

Fig. 1. (a) ATR-FTIR spectra NC coatings deposited from dispersions of oleate-capped ZnO NPs at concentrations of 0.5, 3 and 5 wt % in a n-octane/1,7-octadiene mixture ([1,7-octadiene] = 0.5 vol %). (b) ZnO loading in the NC coating as a function of the NPs concentration in the starting dispersion. (c) Mass deposition rates of the NC coatings and of the coating inorganic and organic components as a function of the NPs concentration in the starting dispersion.

Fig. 2. (a) High resolution XPS C 1s, O 1s and Zn 2p spectra of the nanocomposite coating deposited from a 3 wt % oleate-capped ZnO NPs dispersion in a n-octane/1,7-octadiene mixture ([1,7-octadiene] = 0.5 vol %). (b) XRD patterns of the oleate-capped ZnO NPs and of

the NC coating deposited from a 3 wt % oleate-capped ZnO NPs dispersion in a n-octane/1,7-octadiene mixture ([1,7-octadiene] = 0.5 vol %).

Fig. 3. Top-view (left) and cross-sectional (right) SEM images of NC coatings deposited from dispersions at different concentrations of oleate-capped ZnO NPs in a n-octane/1,7-octadiene mixture: (a) 0.5 wt %, (b) 5 wt % ([1,7-octadiene] = 0.5 vol %, deposition time = 10 min).

Fig. 4. SEM (left) and dark-field TSEM (right) images of typical NPs agglomerates in NC coatings deposited from 3 wt % oleate-capped ZnO NPs dispersions in n-octane/1,7-octadiene mixtures at different 1,7-octadiene concentrations: (a) 0.5 vol %, (b) 2 vol %, (c) 10 vol % (deposition time = 1 min, EHT = 20 kV).

Fig. 5. (a) ZnO loading in the NC coating, (b) mass deposition rates of the NC coating and of the coating inorganic and organic components as a function of the 1,7-octadiene concentration in the n-octane/1,7-octadiene solvent mixture of the starting dispersion ([oleate-capped ZnO NPs] = 3 wt %, deposition time = 10 min).

Fig. 6. Cross-sectional SEM images of NC coatings deposited from dispersions characterized by different 1,7-octadiene concentrations in the HC solvent mixture: (a) 0 vol %, i.e., pure n-octane, (b) 1 vol %, (c) 3 vol %, (d) 10 vol %. (e) RMS roughness and (f) advancing and receding WCAs of the NC coatings as a function of the 1,7-octadiene concentration in the HC mixture ([oleate-capped ZnO NPs] = 3 wt %, deposition time = 10 min).

Fig. 7. (a) RMS roughness and (b) advancing and receding WCAs as function of the ZnO loading in the NC coatings deposited in this work by using DBDs fed by He and the aerosol of dispersions of oleate-capped ZnO NPs in n-octane/1,7-octadiene solvent mixtures.
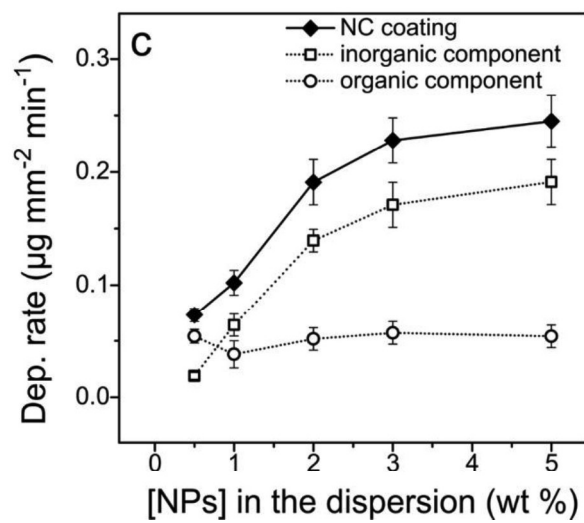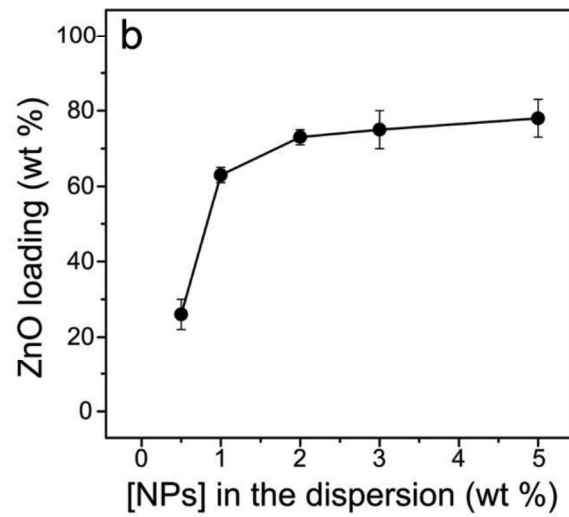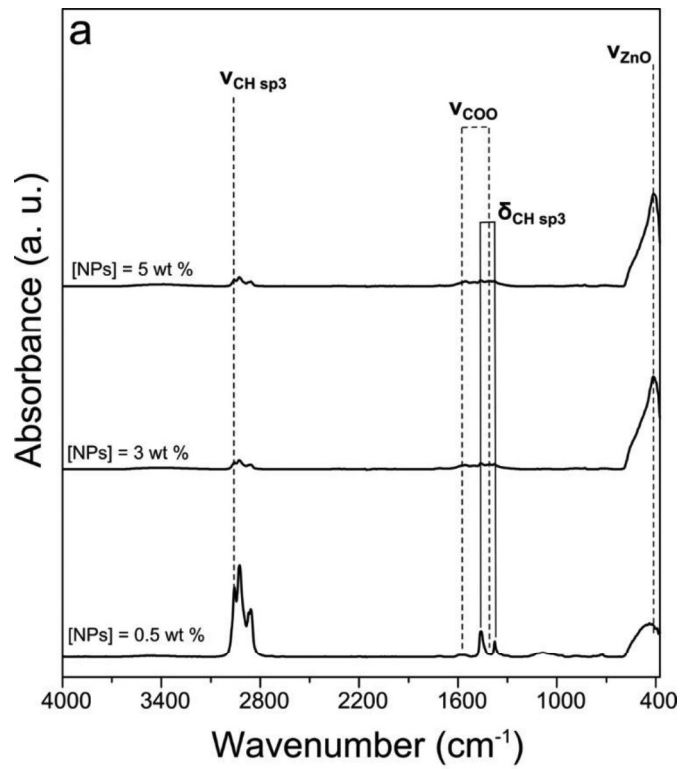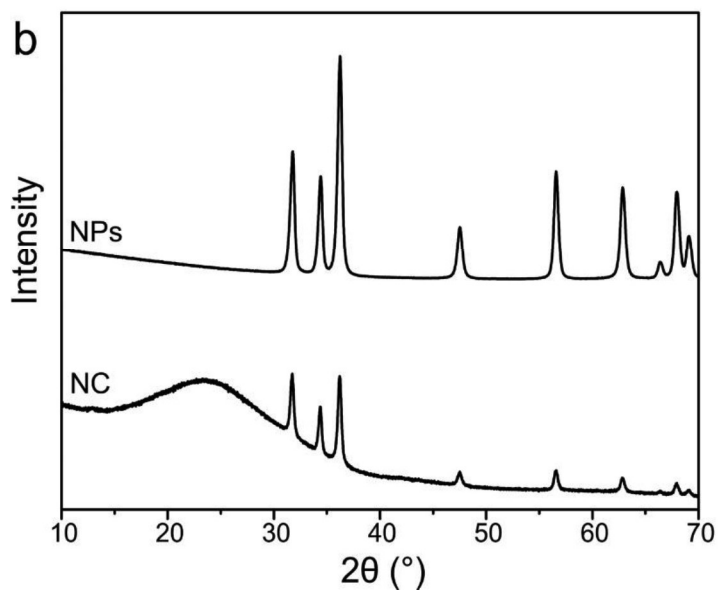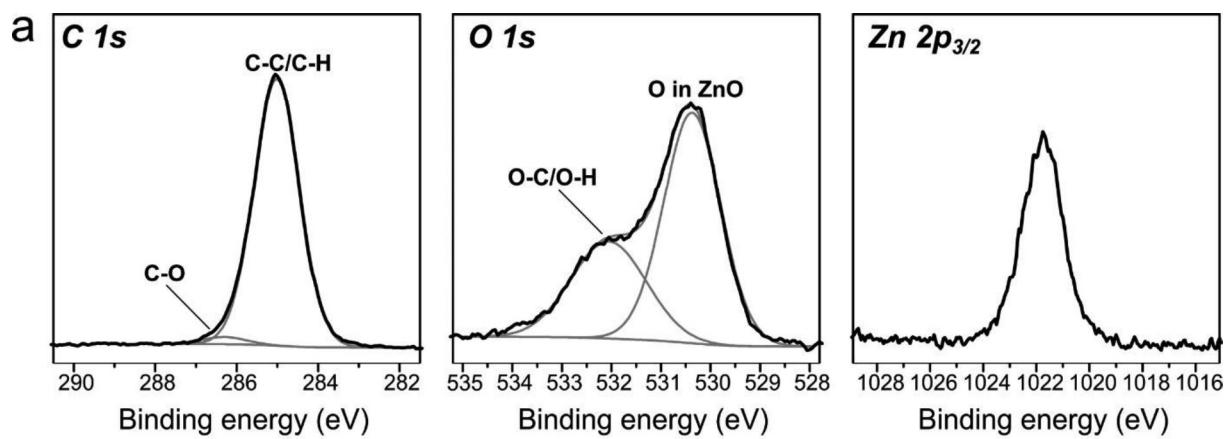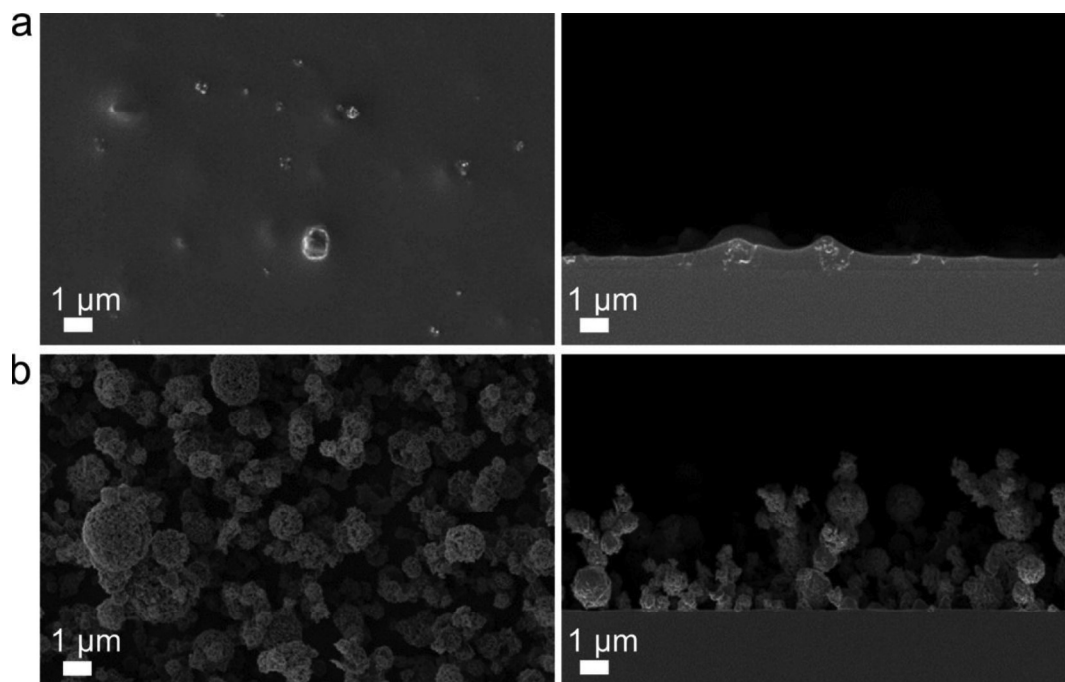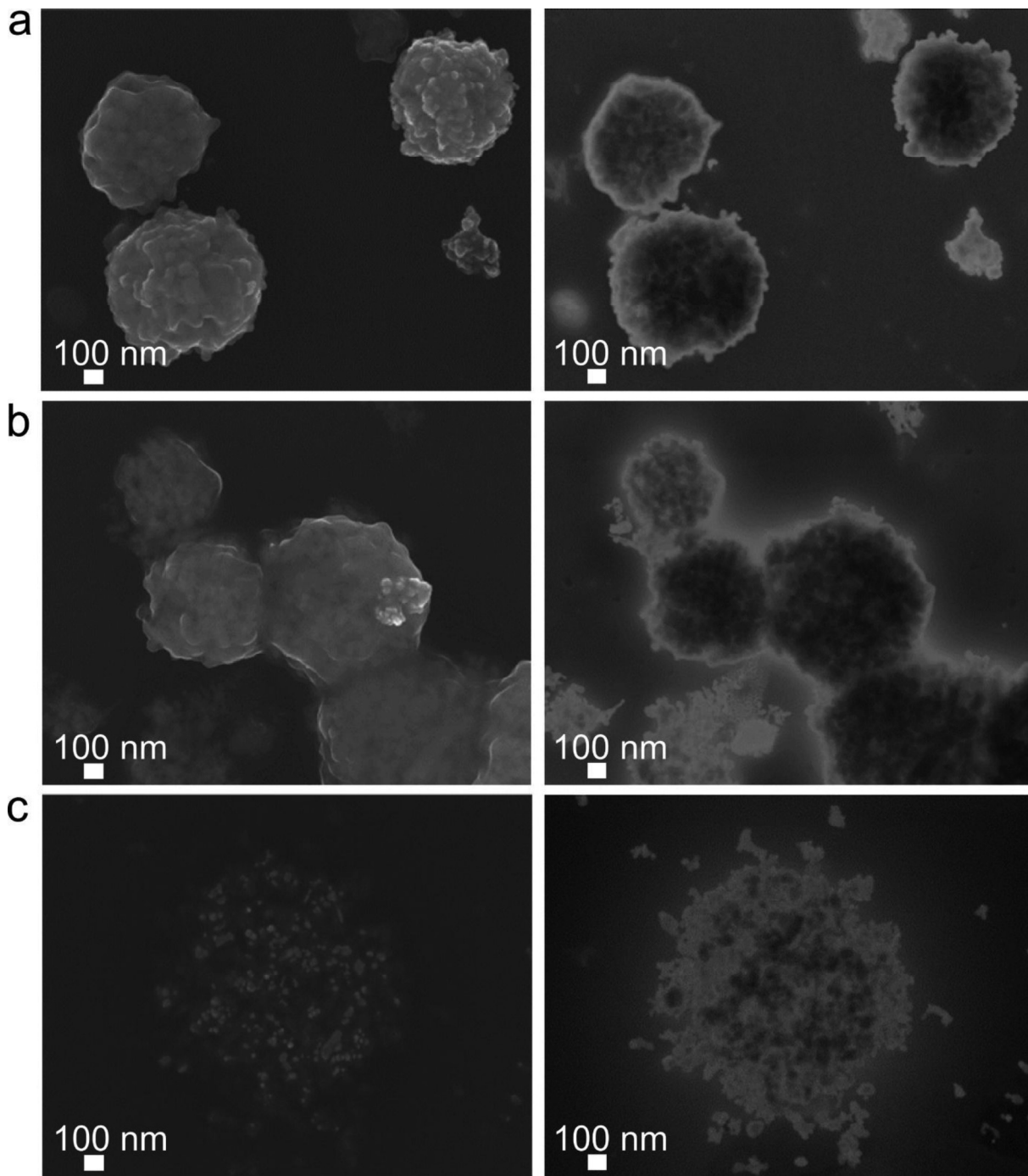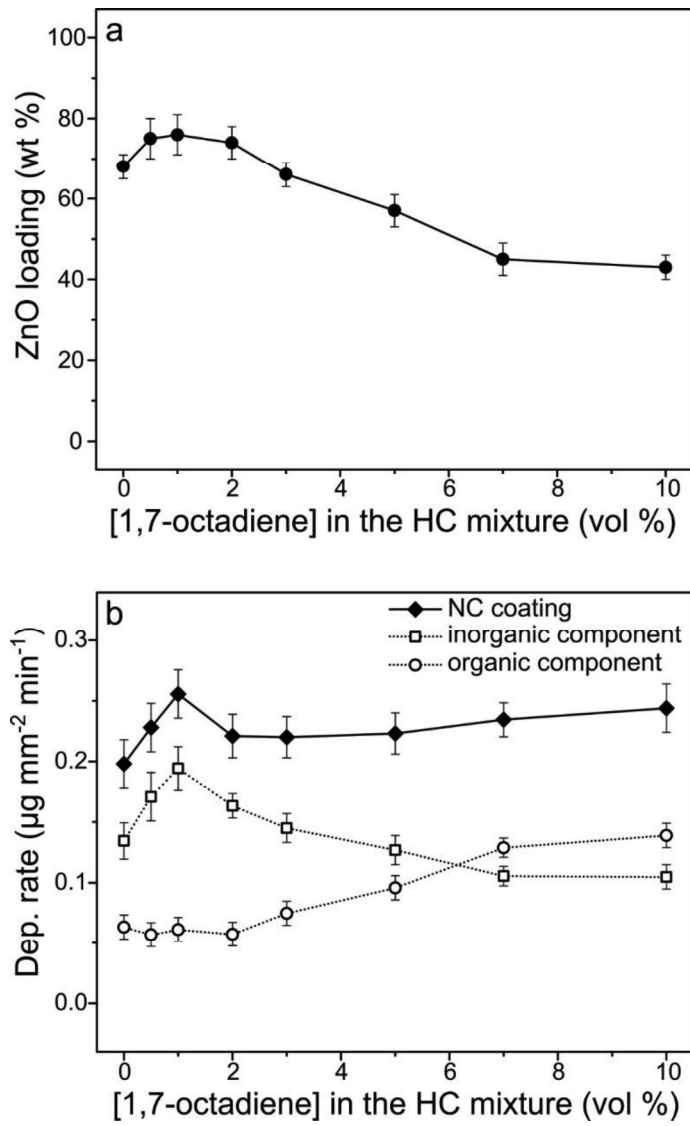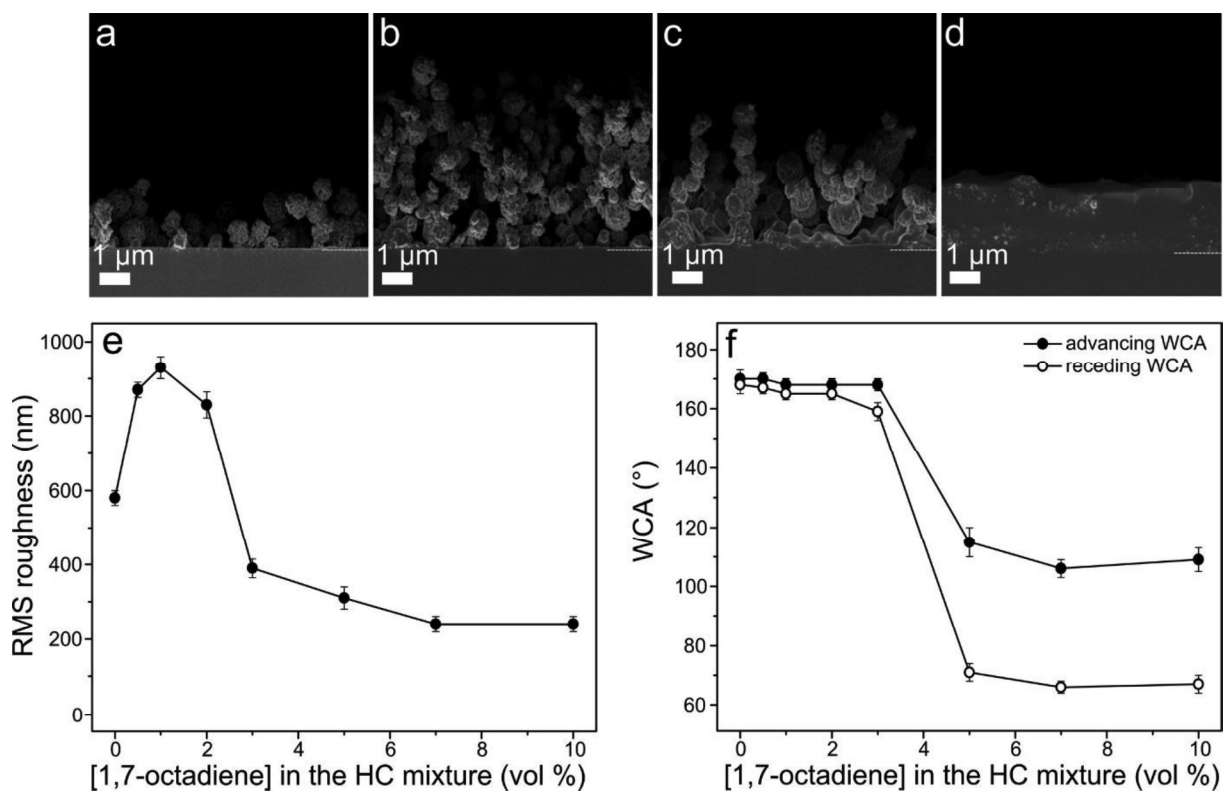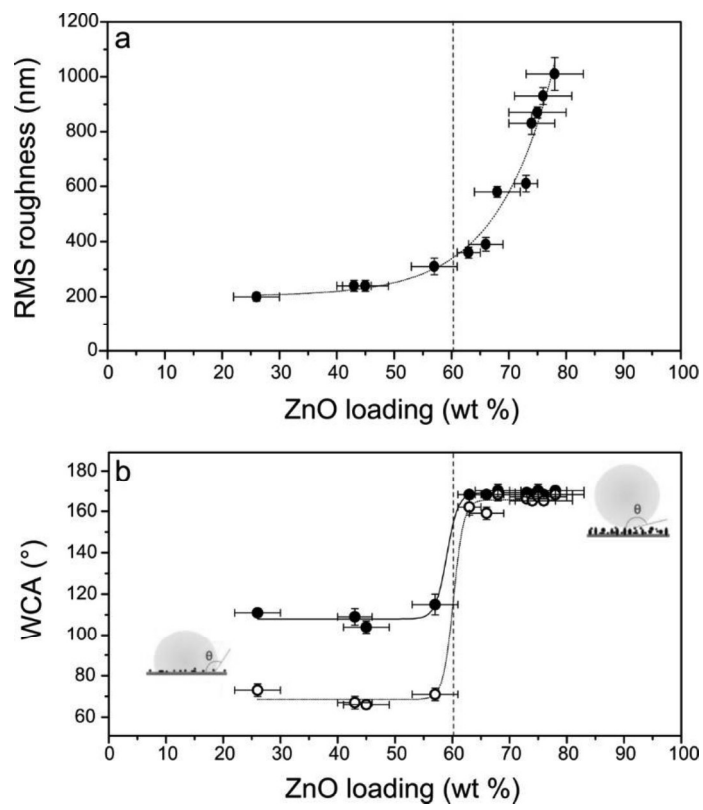
Fig. 1

Fig. 2

a

b

Fig. 3

Fig. 4

Fig. 5

Fig. 6

Fig. 7 (color online only)